CIRP Annals - Manufacturing Technology 73 (2024) 281–284

Contents lists available at ScienceDirect

CIRP Annals - Manufacturing Technology

journal homepage: https://www.editorialmanager.com/CIRP/default.aspx

Flexure-based torque and thrust force drilling dynamometer with Hall effect sensor displacement measurement

Ross Zameroski[a], Christoph Ramsauer[b], Christoph Habersohn[b], Friedrich Bleicher (2)[b], Tony Schmitz (2)[a,c,*]

[a] Machine Tool Research Center, University of Tennessee Knoxville, Knoxville, TN, USA
[b] TU Wien, Vienna, Austria
[c] Manufacturing Science Division, Oak Ridge National Laboratory, Oak Ridge, TN, USA

ARTICLE INFO

Article history:
Available online 7 May 2024

Keywords:
Drilling
Force
Torque

ABSTRACT

This paper describes the design and testing for a low-cost, table-mounted drilling torque and thrust force dynamometer. A flexure-based (constrained-motion) design is detailed, where the rotation for torque and translation for thrust force are measured using a dual magnet-Hall effect sensor configuration that provides a linear voltage output. Two sensors are implemented for each direction to reject undesired structural dynamics. Validation experiments for torque and thrust force are reported using a commercially available, spindle-mounted rotating dynamometer. Results are provided for blind hole drilling in aluminum and stainless steel samples using two drill diameters and various feed rates.

1. Introduction

Low-cost, low-power, high-fidelity sensors are a key capability for improvements in industrial automation and control. Application sectors include automotive, medical, aerospace, and agriculture manufacturing, to name a few [1–3]. In aerospace, for example, the desire to reduce time and cost while drilling metals, composites, and metal-composite structures demands smart drilling solutions with in-process torque/thrust force measurement [4]. Continuous improvement is necessary because millions of holes are necessary for aerospace structure assembly, including riveted and bolted joints [5,6].

This paper describes a low-cost drilling dynamometer for torque and thrust force measurement. Its design is based on rotational and linear flexure kinematics with displacement measurements by four Hall effect sensors using a dual magnet arrangement. The drilling dynamometer concept builds on recent milling dynamometer designs that also implement flexures, while measuring displacements optically [7–10].

Prior drilling dynamometer research includes a strain gauge dynamometer with octagonal ring transducers by Karabay [11,12]. Venkataraman et al. [13] presented a dynamometer where the force and torque were measured using strain gauges fixed to four spokes of a workpiece mounting stage. Byrne and O'Donnell [14] integrated two piezoelectric force sensor rings into the spindle for in-process monitoring. Lee et al. [15] developed a strain gauge dynamometer to measure torque in micro-drilling operations. Li et al. [16] presented a three-component piezoelectric dynamometer to measure the forces during deep hole drilling in optical glass. Totis et al. [17] described a dynamometer based on three triaxial piezoelectric force sensors arranged in a triangular configuration and clamped between two plates.

2. Design description

A flexure-based (constrained-motion) design was selected in this work, where the drilling torque is determined from the rotational displacement of the workpiece mounting stage and the drilling thrust force is determined from the translational displacement of the platform. Fig. 1 displays the constrained-motion drilling dynamometer (CMDD) design. The mounting stage is radially supported by 10 flexure elements (labeled "Spoke" in Fig. 1) that provide rotational, θ, compliance about the vertical axis. The platform is supported by four flexure elements (labeled "Leaf") that provide vertical, z, compliance. These configurations preferentially allow motion in the compliant direction, while

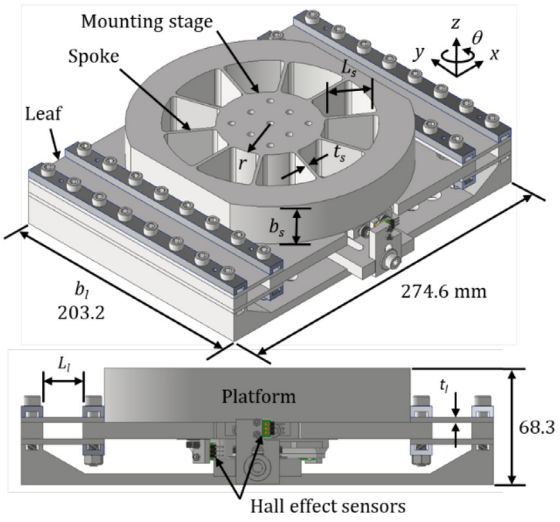

Fig. 1. Drilling dynamometer design.

* Corresponding author.
E-mail address: tony.schmitz@utk.edu (T. Schmitz).

https://doi.org/10.1016/j.cirp.2024.04.086
0007-8506/

restricting motion in other directions. The mounting stage and platform displacements are measured using Hall effect sensors and then scaled by the corresponding stiffness to calculate the drilling torque and thrust force.

The monolithic platform was fabricated from 6061-T6 aluminum (elastic modulus, E, of 69 GPa and yield strength, σ_y, of 276 MPa) The rotational stiffness, K_θ, of the mounting stage is given by Eq. (1), where N_s is the number of spokes, I_s is the second moment of area for the rectangular spoke cross-section, L_s is the spoke length in the radial direction, b_s is the spoke width, t_s is the spoke thickness, and r is the mounting stage radius [18].

$$K_\theta = 4N_s EI_s\left(\frac{1}{L_s}+\frac{3r}{{L_s}^2}+\frac{3r^2}{{L_s}^3}\right)=\frac{N_s E b_s {t_s}^3}{3}\left(\frac{1}{L_s}+\frac{3r}{{L_s}^2}+\frac{3r^2}{{L_s}^3}\right) \quad (1)$$

The vertical displacement is enabled by four 6061-T6 aluminum flexure elements arranged in a parallelogram configuration. The (vertical) translational stiffness, K_z, is given by Eq. (2), where I_l is the second moment of area for the rectangular leaf cross-section, L_l is the leaf length, b_l is the leaf width, t_l is the leaf thickness, and N_l is the number of flexure elements [19].

$$K_z = N_l\frac{12EI_l}{{L_l}^3}=N_l E b_l\left(\frac{t_l}{L_l}\right)^3 \quad (2)$$

Because the rotational and translational stiffnesses are strongly dependent on the flexure element thickness and length, contour plots were generated to show lines of constant stiffness as a function of these key design parameters. See Fig. 2, where the red circles identify the design combinations and corresponding stiffnesses. The flexure element dimensions and stiffnesses are summarized in Table 1.

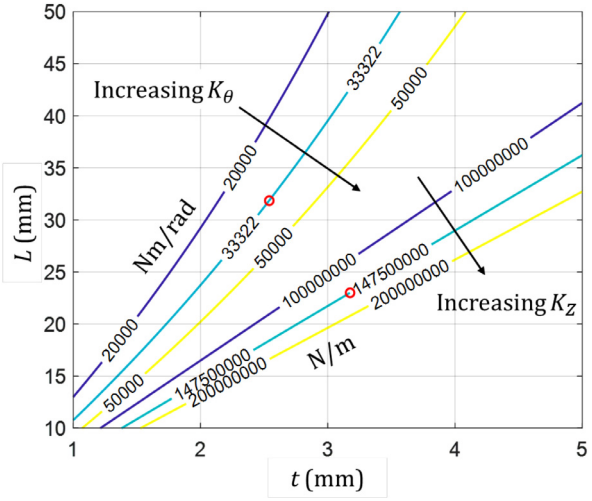

Fig. 2. Lines of constant stiffness based on spoke and leaf thickness (t) and length (L). For rotational stiffness, K_θ (Nm/rad), the axes represent spoke dimensions. For translational stiffness, K_z (N/m), the axes represent leaf dimensions.

Table 1
CMDD design dimensions and stiffness values.

Mounting stage				
L_s (mm)	b_s (mm)	t_s (mm)	r (mm)	K_θ (Nm/rad)
31.85	31.75	2.540	38.10	3.33×10^4
Platform				
L_l (mm)	b_l (mm)	t_l (mm)		K_y (N/m)
23.00	203.2	3.175		1.48×10^8

Finite element analysis, FEA (ANSYS Workbench), was also used to predict the rotational and translational stiffnesses. For the rotational static stiffness, a 1 Nm moment was applied to the central axis of the mounting stage and the rotation was recorded at the outer diameter of the mounting stage. The rotational stiffness was determined by dividing the moment by the predicted rotation. The translational stiffness was predicted from the vertical deflection of the mounting stage due to a 1 N vertical force applied to the top center of the mounting stage. To enable direct comparison to the analytical results, the mounting stage was modeled as rigid so its compliance would not contribute to the deflection; see Table 2. In practice, the mounting stage compliance reduces the translational stiffness. When considering the complete drilling dynamometer model, the equivalent translational stiffness predicted by FEA was $K_{z,eq} = 6.75\times10^7$ N/m.

Table 2
Comparison of analytical and FEA stiffnesses (rigid platform).

K_θ (Nm/rad)		
Analytical	FEA	Percent difference (%)
3.33×10^4	3.30×10^4	−1.04
K_z (N/m)		
1.48×10^8	1.63×10^8	9.20

To evaluate frequency separation between the vibration modes, modal finite element simulations were performed; see Table 3. It was observed that the first mode natural frequency (platform vertical displacement) was closely spaced to the second mode natural frequency (platform tilting). However, the effects of the second mode are minimized using two Hall effect sensors which are positioned so that, when the responses are averaged, the influence of the second mode is ideally rejected. The third mode (mounting stage rotation) was sufficiently separated from the other modes to enable a single degree of freedom approximation for the rotational dynamics. Two Hall effect sensors are also used to measure the rotational response and their results are averaged.

Table 3
CMDD vibration modes.

Natural freq.	Description
892 Hz	Platform vertical displacement (intended)
962 Hz	Platform out-of-plane tilt
1448 Hz	Mounting stage rotation (intended)
1605 Hz	Platform out-of-plane tilt
2558 Hz	Platform twist

3. Sensor selection

Hall effect sensors detect the presence and magnitude of a magnetic field by measuring a voltage difference induced by the magnetic field across an electrical conductor. The magnitude of the voltage difference is directly proportional to the magnetic field strength. Bipolar Hall effect sensors are applied here to measure the mounting stage and platform displacements. A dual magnet, opposite pole configuration is implemented so that, when the magnets translate across the sensing element, the response varies linearly from the low to high voltage saturation levels. Sensor-magnet combinations were evaluated using an air bearing stage (Aerotech ABL 10100-LT) with 0.2 µm positioning uncertainty and 0.5 nm resolution. A Texas Instruments DRV5055A2 Hall effect sensor and two N52 gold-plated neodymium disc magnets provided the required performance; see Fig. 3. This combination had a linear range of 250 µm and a sensitivity of 36.8 µm/V (0.2 mm sensor-magnet air gap).

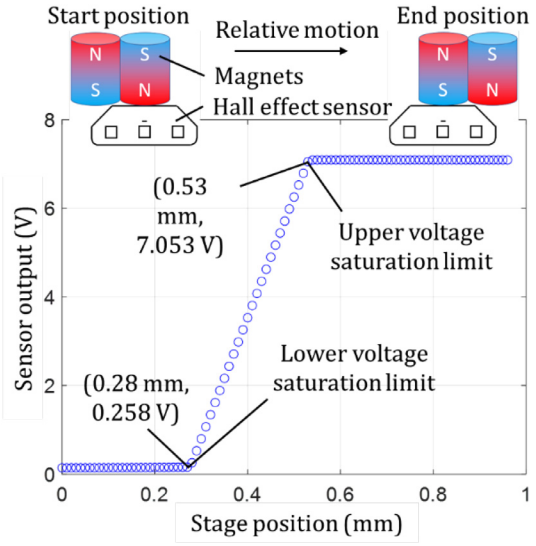

Fig. 3. Calibration curve for selected Hall effect sensor and magnets.

Given the calibrated sensor, the measurable torque, T, range is calculated by multiplying the rotational stiffness by the rotation, θ, as shown in Eq. (3). The rotation is determined by dividing the mounting stage displacement, x, by the

sensor's distance from the stage center, d, (i.e., applying the small angle approximation). The displacement is the product of the sensitivity, S, and sensor output voltage, V. The measurable thrust force, F, is calculated using Eq. (4), where z is the platform displacement. For a sensor noise level of 0.005 V and d value of 51.7 mm, the maximum and minimum measurable T values are 166.6 Nm and 0.1 Nm and the maximum and minimum measurable F values are 16,875 N and 12.4 N.

$$T = K_\theta \theta = K_\theta \frac{x}{d} = K_\theta \frac{SV}{d} \tag{3}$$

$$F = K_{z,eq} z = K_{z,eq} SV \tag{4}$$

4. Initial testing

The predicted rotational stiffness value was validated using a prototype CMDD. The stiffness was measured by clamping the CMDD to a machining center table, applying a known torque using a hanging mass at a selected radius, measuring the rotation using the Hall effect sensors, and calculating the stiffness; see Fig. 4. Holes in the mounting stage were organized in three rows (1–3) and three columns (A-C) to enable measurements at multiple locations. Five masses (1.030 kg to 4.688 kg) were selected. For each hole-mass combination, the change in voltage was recorded by both Hall effect sensors and converted to rotation using each sensor's sensitivity and radial distance from the mounting stage center. The applied force was converted to torque by multiplying by the radius. The applied torque was divided by the measured rotations to obtain two stiffness values, which were averaged to obtain the final stiffness. The average value from all measurements was calculated and used to represent the CMDD behavior. The result was 3.17×10^4 Nm/rad with a standard deviation of 935 Nm/rad (4.8 % less than the analytical solution and 3.8 % less than the FEA solution in Table 2).

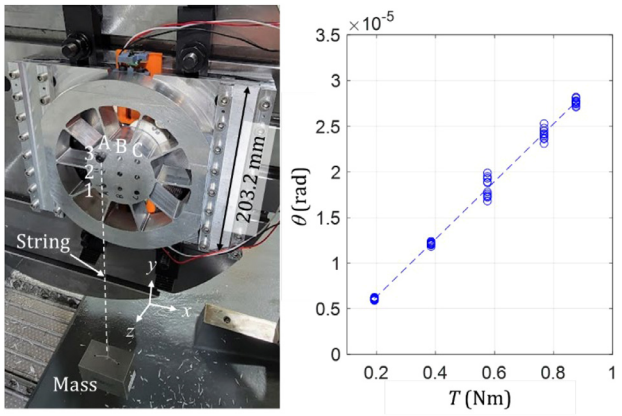

Fig. 4. Static rotational stiffness experimental setup. (Left) 3-A torque application location. (Right) Calibration data and least square fit.

Prior to performing drilling experiments, damping inserts were fabricated from thermoplastic polyurethane (TPU) using fused filament fabrication and placed between the spokes to increase damping and provide shielding for the sensors. The validation experiments were repeated to examine how the inclusion of the inserts affect the static rotational stiffness. The static rotational testing procedure was repeated with the damping inserts in place. In this case, the average value from all measurements was 3.36×10^4 Nm/rad (5.9 % larger than without the damping inserts) with a standard deviation of 820 Nm/rad.

The translational stiffness was validated using mass loading. The stiffness was measured by fixing the CMDD to the table of a five-axis CNC machining center, placing a known mass on the center of the mounting stage, and measuring the platform deflection using the Hall effect sensors. Eddy current displacement sensors (Micro-epsilon EPU05-C3-A/M) were also deployed for comparison. Six masses, ranging from 3.069 kg to 10.388 kg, were used to apply the thrust force. The measured displacements were averaged and plotted against the applied force. The slope of the best fit line was 1.93×10^{-8} m/N, which corresponds to a translational stiffness of 5.18×10^7 N/m (26.3 % less than compliant platform FEA solution).

5. Commercial dynamometer comparison

Drilling tests were conducted to compare CMDD results to those obtained from a commercially available, rotating dynamometer (Kistler 9170A1312). Two workpiece materials (6060 aluminum and DIN EN 1.4301 stainless steel) were selected and the samples were bolted to the CMDD. Blind hole drilling tests were performed with 8 mm and 12 mm diameter, two flute, solid carbide, TiAlN coated drills with 140° point angles (Kennametal 1913487 and 1913502). The drilling parameters are shown in Table 4. The drilling tests were completed using a DMG-Mori DMU 75 monoBLOCK five-axis CNC machining center. A Stoddard solvent (WD-40) was applied to the workpiece surface prior to drilling to prevent the chips from adhering to the tool. A center drilling operation was performed prior to the blind hole drilling tests; see the setup in Fig. 5. To evaluate repeatability, three holes were drilled for each parameter combination.

Table 4
Drilling parameters.

Material	6060 aluminum		1.4301 stainless steel	
Dia. (mm)	8	12	8	12
Feed (mm/min)	573, 716, 860	572, 764	143, 191	127, 170
Spindle speed (rpm)	3581	2387	1592	1061
Depth (mm)	12	18	12	12

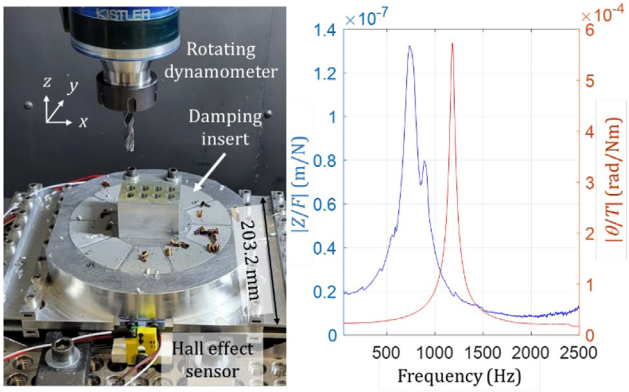

Fig. 5. (Left) Drilling setup on a DMG-Mori DMU 75 with an aluminum sample bolted to the CMDD mounting stage. The drill is clamped in the rotating dynamometer. (Right) Measured frequency response functions.

The drilling torque and thrust force were sampled at 20 kHz and the mean values were determined from the steady-state portion of each test; see Fig. 6. For a given parameter set, the three mean values were averaged to report the drilling torque and thrust force; standard deviations of the steady-state signals were calculated to express uncertainty. Comparisons of drilling torque and

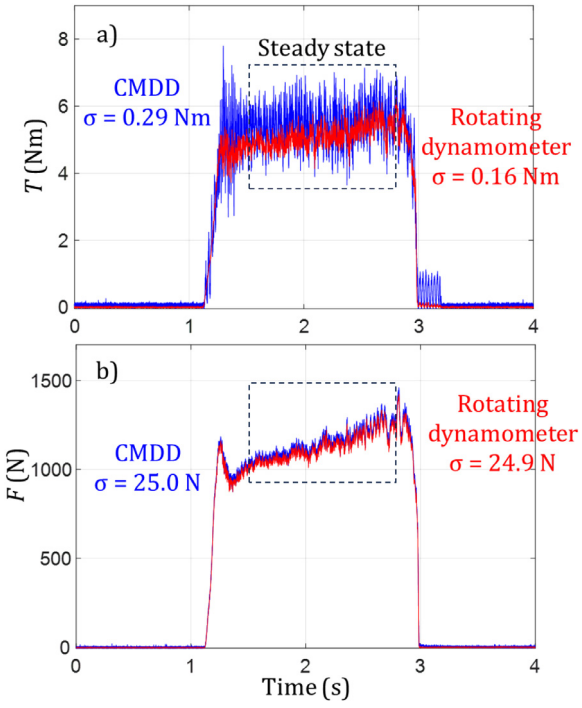

Fig. 6. Time domain a) torque and b) thrust force signals.

thrust force values are displayed in Figs. 7 and 8. It is observed in Fig. 7 that the CMDD drilling torque demonstrates overlapping error bars with the rotating dynamometer and mean values that differ by 8.2 % or less. In Fig. 8, the CMDD thrust force again demonstrates overlapping error bars with the rotating dynamometer and the maximum difference is 7.9 %.

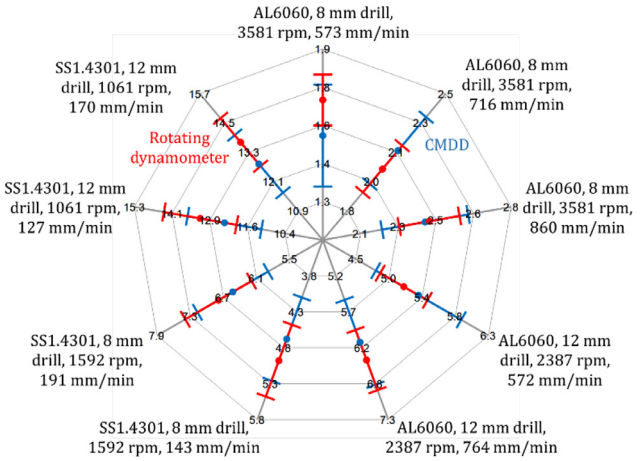

Fig. 7. Radar chart comparing the CMDD and rotating dynamometer drilling torque (Nm). Each radial axis represents a combination of drilling parameters and the error bars represent two standard deviations (95 % confidence interval). Note the change in scale along each axis.

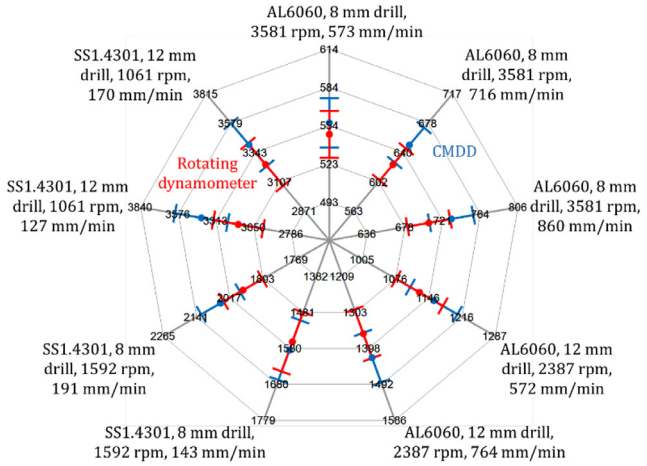

Fig. 8. CMDD and rotating dynamometer thrust force (N) comparison.

6. Conclusions

This paper described a drilling dynamometer for torque and thrust force measurement with rotational and linear flexure kinematics (US $650 supplies cost). Displacement measurements were performed using two pairs of dual magnet-Hall effect sensors. The opposite pole arrangement of the magnets provided a linear response over the full sensor range, while the sensor pairs enabled the rejection of undesired structural dynamics. Torque and thrust force measurement results were presented for both the constrained-motion drilling dynamometer (CMDD) and a commercially available rotating dynamometer. A comparison of the two dynamometers from multiple drilling conditions showed a maximum percent difference of 8.2 % for torque and 7.9 % for thrust force; overlapping error bars were observed in all cases. Future work will include additional calibration studies (e.g., the CMDD consistently measured higher thrust force) and design refinements to reduce the CMDD footprint.

Declaration of competing interest

The authors declare that they have no known competing financial interests or personal relationships that could have appeared to influence the work reported in this paper.

CRediT authorship contribution statement

Ross Zameroski: Data curation, Formal analysis, Investigation, Methodology, Validation, Visualization, Writing – original draft. **Christoph Ramsauer:** Data curation, Investigation, Validation, Writing – review & editing. **Christoph Habersohn:** Data curation, Investigation, Software, Supervision, Validation, Writing – review & editing. **Friedrich Bleicher:** Conceptualization, Funding acquisition, Investigation, Project administration, Resources, Supervision, Validation, Writing – original draft, Writing – review & editing. **Tony Schmitz:** Conceptualization, Data curation, Formal analysis, Funding acquisition, Investigation, Methodology, Project administration, Supervision, Validation, Visualization, Writing – original draft, Writing – review & editing.

Acknowledgements

The authors acknowledge financial support from the Austrian Marshall Plan Foundation and equipment support from the Machine Tool Technologies Research Foundation (MTTRF).

Supplementary materials

Supplementary material associated with this article can be found in the online version at doi:10.1016/j.cirp.2024.04.086.

References

[1] Schütze A, Helwig N, Schneider T (2018) Sensors 4.0-Smart Sensors and Measurement Technology Enable Industry 4.0. *Journal of Sensors and Sensor Systems* 7 (1):359–371.
[2] Kalsoom T, Ramzan N, Ahmed S, Ur-Rehman M (2020) Advances in Sensor Technologies in the Era of Smart Factory and Industry 4.0. *Sensors* 20(23):6783.
[3] Javaid M, Haleem A, Singh RP, Rab S, Suman R (2021) Significance of Sensors for Industry 4.0: Roles, Capabilities, and Applications. *Sensors International* 2:100110.
[4] Araujo AC, Landon Y, Lagarrigue P (2021) Smart Drilling for Aerospace Industry: State of Art in Research and Education. *Procedia CIRP* 99:387–391.
[5] Aamir M, Tolouei-Rad M, Giasin K, Nosrati A (2019) Recent Advances in Drilling of Carbon Fiber-Reinforced Polymers for Aerospace Applications: A Review. *The International Journal of Advanced Manufacturing Technology* 105:2289–2308.
[6] Aamir M, Giasin K, Tolouei-Rad M, Vafadar A (2020) A Review: Drilling Performance and Hole Quality of Aluminium Alloys for Aerospace Applications. *Journal of Materials Research and Technology* 9(6):12484–12500.
[7] Gomez M, Schmitz T (2020) Low-Cost, Constrained-Motion Dynamometer for Milling Force Measurement. *Manufacturing Letters* 25:34–39.
[8] Gomez M, Honeycutt A, Schmitz T (2021) Hybrid Manufactured Dynamometer for Cutting Force Measurement. *Manufacturing Letters* 29:65–69.
[9] Gomez M, Schmitz T (2022) Stability Evaluation for a Damped, Constrained-Motion Cutting Force Dynamometer. *Journal of Manufacturing and Materials Processing* 6(1):23.
[10] Ramsauer C, Leitner D, Habersohn C, Schmitz T, Yamazaki K, Bleicher F (2023) Flexure-Based Dynamometer for Vector-Valued Milling Force Measurement. *Journal of Machine Engineering* 23.
[11] Karabay S (2007) Analysis of Drill Dynamometer with Octagonal Ring Type Transducers for Monitoring of Cutting Forces in Drilling and Allied Process. *Materials & Design* 28(2):673–685.
[12] Karabay S (2007) Performance Testing of a Constructed Drilling Dynamometer by Deriving Empirical Equations for Drill Torque and Thrust on SAE 1020 Steel. *Materials & Design* 28(6):1780–1793.
[13] Venkataraman R, Lamble JH, Koenigsberger F (1965) Analysis and Performance Testing of a Dynamometer for Use in Drilling and Allied Processes. *International Journal of Machine Tool Design and Research* 5(4):233–261.
[14] Byrne G, O'Donnell GE (2007) An Integrated Force Sensor Solution for Process Monitoring of Drilling Operations. *CIRP Annals - Manufacturing Technology* 56 (1):89–92.
[15] Lee KE, Kim JW, Kim CY, Ahn SH (2009) Development of Micro Torque Measurement Device Using Strain Gauge. *2009 IEEE International Symposium on Assembly and Manufacturing*, IEEE, 101–106.
[16] Li X, Zhang J, Ren Z, Lu W (2023) Development of the Piezoelectric Dynamometer for Brittle Material Drilling. *Journal of the Chinese Institute of Engineers* 46(1):53–62.
[17] Totis G, Adams O, Sortino M, Veselovac D, Klocke F (2014) Development of an Innovative Plate Dynamometer for Advanced Milling and Drilling Applications. *Measurement* 49:164–181.
[18] Tsetserukou D, Tadakuma R, Kajimoto H, Tachi S (2006) Optical Torque Sensors for Implementation of Local Impedance Control of the Arm of Humanoid Robot. In: *Proceedings 2006 IEEE International Conference on Robotics and Automation, 2006. ICRA 2006*, IEEE, 1674–1679.
[19] Smith ST (2000) *Flexures: Elements of Elastic Mechanisms*, CRC Press.